[Supplementary materials]

Luffa cylindrica-inspired powerless micropump: long-term, high-flow operation and energy-generation application

Jungjae Woo[1], Jeongmin Seo[1], Hyewon Cho[1], Soeun Park[1], Changsoo Han[1], Hyejeong Kim[1,2,†]

[1] School of Mechanical Engineering, Korea University, Seoul 02841, Republic of Korea

[2] Max Planck Institute for Dynamics and Self-Organization, Am Faßberg 17, 37077 Göttingen, Germany

[†] Corresponding author

e-mail: h_kim@korea.ac.kr

phone: +82-2-3290-3379

Keywords: Luffa cylindrica, Aerogel, Powerless micropump, Water absorption, Reverse electrodialysis

Supplementary materials

Contents of supplementary materials

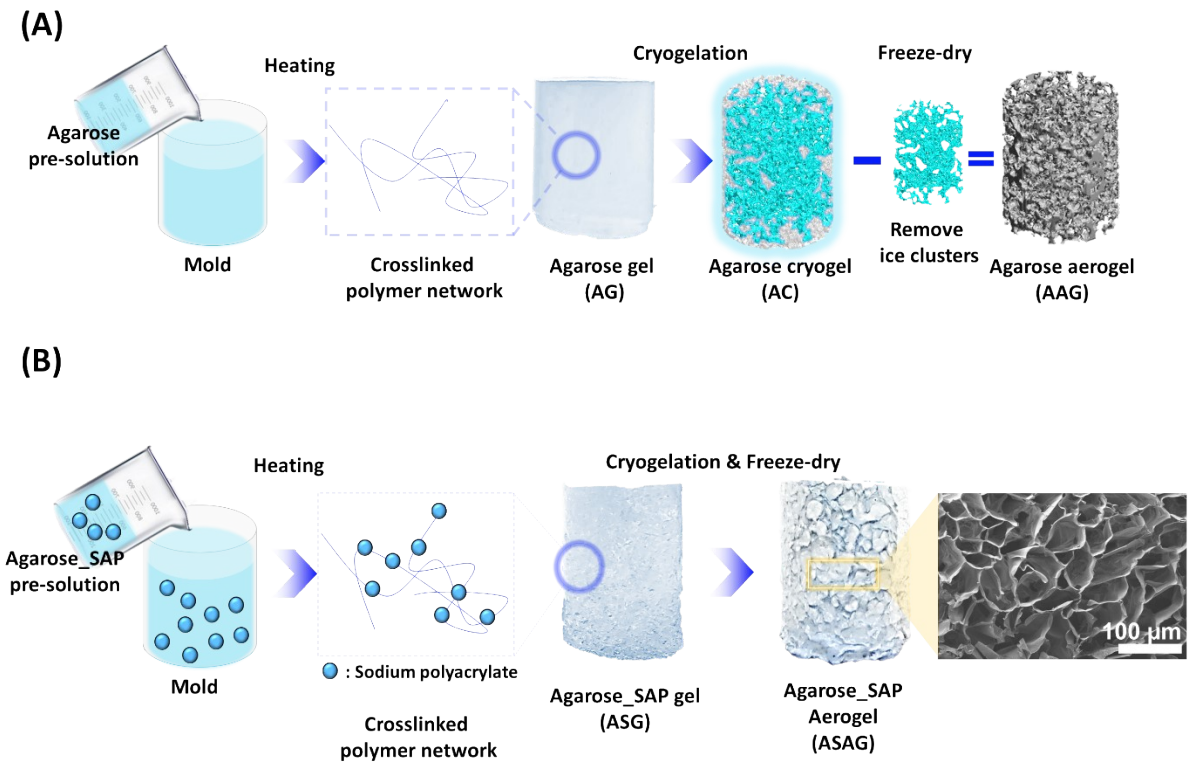

Figure S1. Fabrication method of (A) AAG and (B) ASAG.

S1. Fabrication steps of AAG and ASAG

Agarose gels (AG) were prepared at a concentrations of 2 wt% relative to the total volume of DI water. The agarose was pre-mixed with DI water and heated until fully dissolved (Fig. S1A). Subsequently, 18 mL of the heated agarose solution was cast into 3D-printed molds of various shapes to produce different AG geometries (cylinders and cones). The cylinder-shaped micropump had a diameter and height of 24 and 40 mm, respectively, while the cone-shaped micropump had a height and an upper diameter of 20 and 56 mm, respectively. After complete gelation at room temperature, the AG underwent cryogelation at -17 ℃ for 2 h, resulting in agarose cryogels (AC) with macro-scale pores. During cryogelation, ice clusters were formed within the AG. These clusters subsequently developed into the macro pores during a freeze-drying process at -48.5 ℃±1.12 ℃ for 48 h, which effectively removed all moisture, resulting in the formation of AAG.

To fabricate the ASAG, 2 wt% AAG was selected as the base material for favorable water permeability of the micropump. Additionally, 0.1 wt% sodium polyacrylate was pre-mixed with the 2 wt% agarose solution before heating, following the same procedure of cryogelation and freeze drying as described above (Fig. S1B). This process resulted in the fabrication of ASAG. Similarly, an ASAG micropump was fabricated by incorporating a cotton resistor into the bottom section.

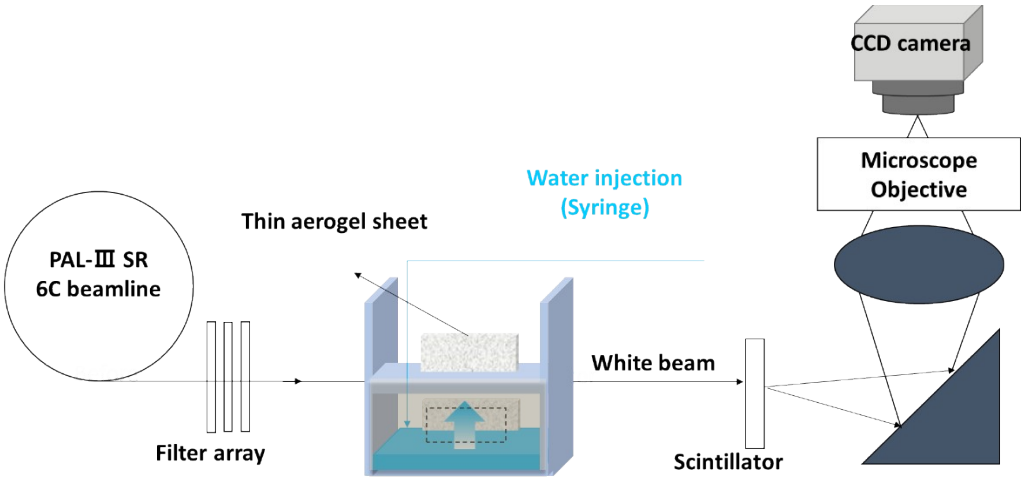

Figure S2. Experimental setup of synchrotron X-ray imaging to visualize water absorption in the AAG.

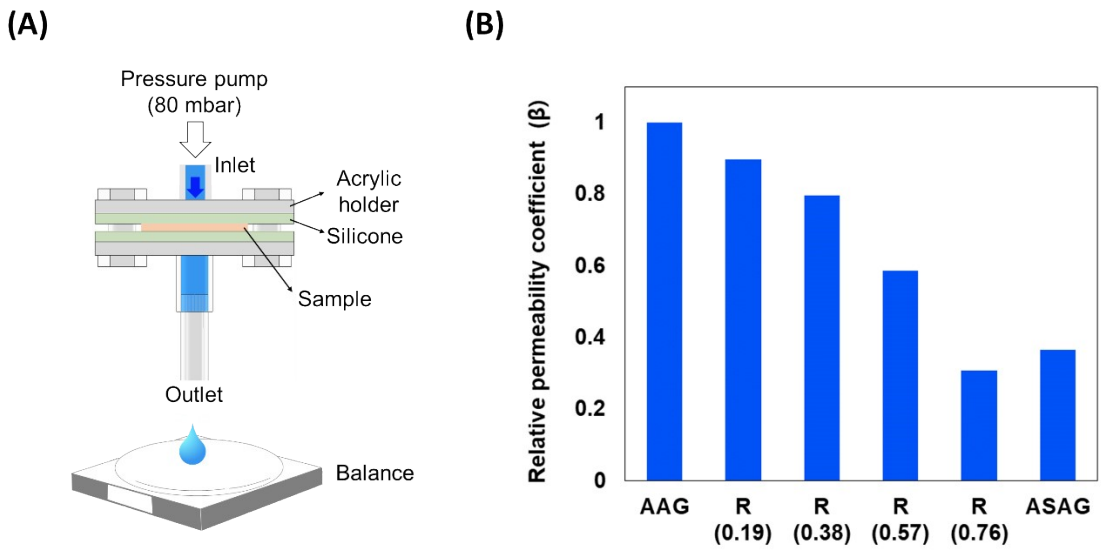

Figure S3. (A) Experimental setup for measuring the water permeability coefficient of aerogels and flow resistors, (B) relative permeability coefficients (β) of AAG, ASAG, and flow resistors with varying densities.

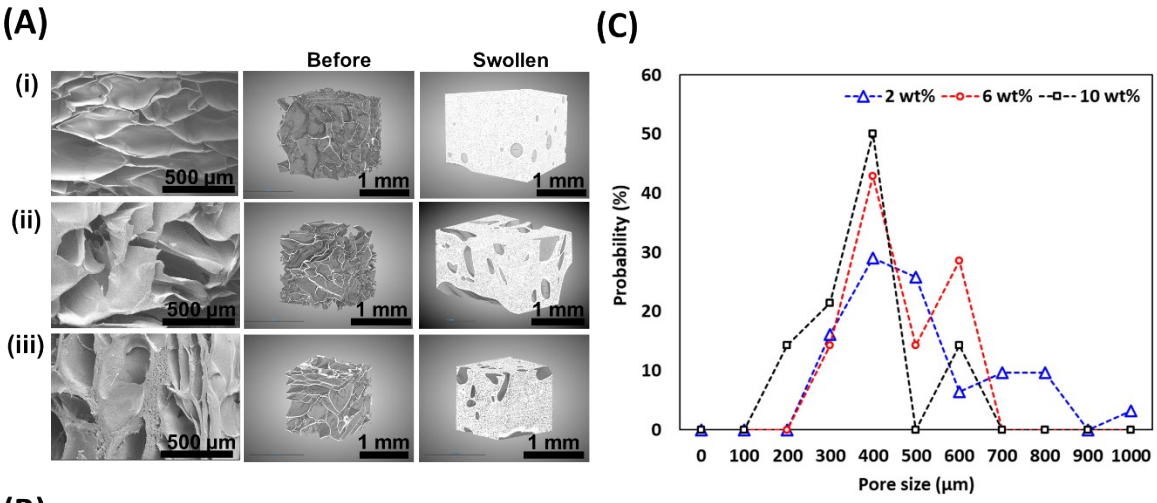

(B)

Gel Conc.	Porosity (ø)	Average pore size (µm)	Min / Max
2 wt%	91.15% (± 1.29%)	463.8 (± 174.3)	210.9 / 982.2
6 wt%	90.87% (± 1.04%)	414.5 (± 103.2)	230.6 / 549.0
10 wt%	85.34% (± 0.49%)	331.5 (± 112.1)	166.0 / 594.0

Figure S4. (A) SEM images of porous structure and 3D structures obtained from X-ray computed tomography for (i) 2 wt%, (ii) 6 wt, and (iii) 10 wt% AAG in dried and swollen states. (B) Porosity, average pore size, and the minimum and maximum pore size of AAG with various concentrations. (C) Pore size distribution of AAG with various concentrations.

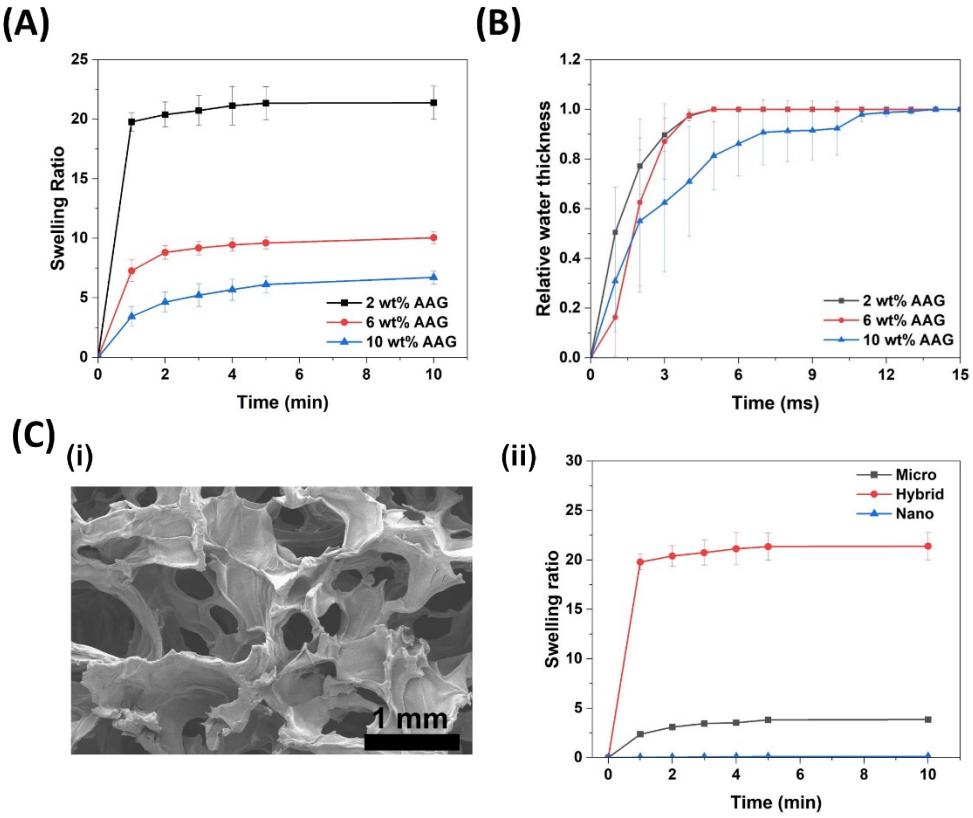

Figure S5. (A) Swelling ratio and (B) relative water thickness according to various concentrations of AAG. (C) (i) Microporous structure of AAG fabricated by sugar leaching method, (ii) swelling ratio for different pore size structure.

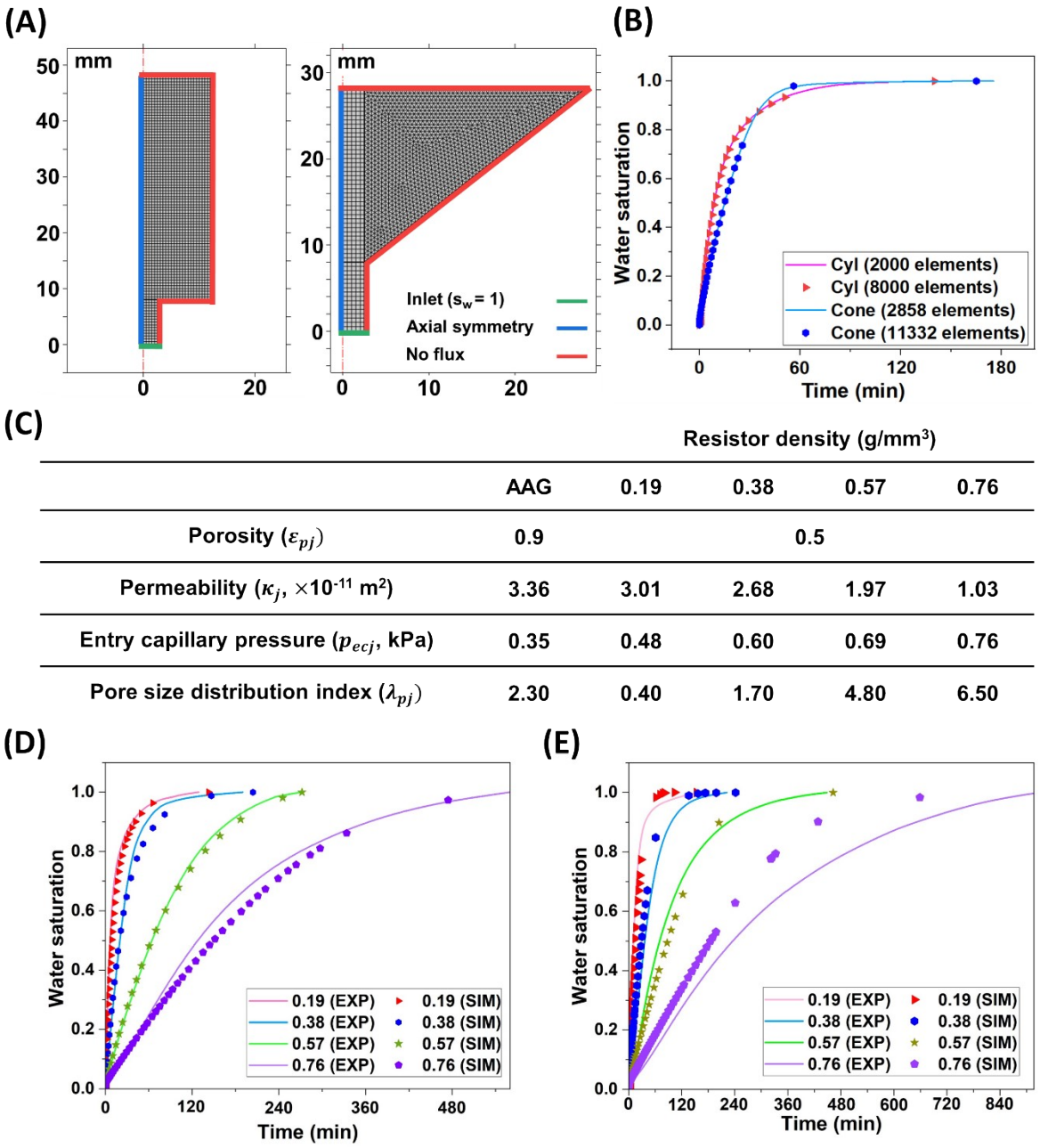

	AAG	0.19	0.38	0.57	0.76
Porosity (ε_{pj})	0.9	0.5			
Permeability (κ_j, $\times 10^{-11}$ m^2)	3.36	3.01	2.68	1.97	1.03
Entry capillary pressure (p_{ecj}, kPa)	0.35	0.48	0.60	0.69	0.76
Pore size distribution index (λ_{pj})	2.30	0.40	1.70	4.80	6.50

Figure S6. Numerical analysis of flow distribution and validation of micropump performance. (A) Mesh representations for cylinder-shaped and cone-shaped micropumps. (B) Evaluation of mesh suitability. (C) Key parameters for numerical analysis derived from the comparison between the simulation and experimental results. (D) Comparison of experimental and simulation results for the cylinder-shaped micropump. (E) Comparison of experimental and simulation results for the cone-shaped micropump.

S6. Numerical analysis of flow distribution in LIM

A 2D axisymmetric geometry was implemented in COMSOL Multiphysics 5.5, utilizing the finite element method (FEM) to model the operation of the micropump. The phase transport in the porous media model was employed to investigate the internal flow dynamics within the pump. The constructed 2D geometry and corresponding mesh are presented in Fig. S6A. Simulations were performed under the initial conditions in which the water-volume fraction was uniformly set to zero throughout the domain, except at the inlet of the flow resistor, where it was fixed at its maximum value of 1. The boundary at r=0 was defined as axially symmetric, and all other domain boundaries except for the inlet and axially symmetric boundaries were assigned no-flux conditions.

The meshes of cylinder-shaped and cone-shaped geometries consisted of 2,000 and 2,858 elements, respectively. For the cylinder-shaped mesh, both the minimum and average mesh qualities were 1.0, indicating a reasonable mesh structure. The results showed the same convergence values even after further increasing the number of mesh elements, confirming its adequacy (Fig. S6B). For the cone-shaped mesh, the minimum quality was 0.6351, whereas the average quality remained high at 0.9516. This mesh also demonstrated the same convergence value as those with more higher elements, indicating a reasonable structure. The simulation was then performed at intervals of 1 s, up to a maximum duration of 55,800 s. The simulation was conducted on an AMD Ryzen Threadripper PRO 3955WX 16-Core CPU with 224 GB RAM, and the calculation times ranged from 26 to 115 s.

For the micropump, the bottom part (flow resistor) was assigned a porosity (ε_{p1}) of 0.5, while the upper part (AAG) had a porosity (ε_{p2}) of 0.9. Initially, the entry capillary pressure (P_{ec1}) was set to 0.35 kPa, calculated using an equation with the determined average pore size (Eq. 8). The permeability values of the AAG and each resistor were derived by scaling the

experimentally measured values (Fig. S3B). The pore-size-distribution index (λ_{p1}) and permeability of AAG were determined to be 2.3 and 3.36×10^{-11} m^2, respectively, by fitting the water-saturation data over time to the experimental results (Fig. S6D). Similarly, the entry capillary pressure (P_{ec2}) and pore-size-distribution index (λ_{p2}) of the resistor with a density of 0.19 g/mm^3 were determined to be 0.48 kPa and 0.4, respectively. The subsequent densities of the flow resistors were scaled by factors of two, three, and four. Accordingly, the entry capillary pressure was adjusted to 1.26 times ($\sqrt[3]{2}$), 1.44 times ($\sqrt[3]{3}$), and 1.59 times ($\sqrt[3]{4}$) of the initial value, respectively. The pore-size-distribution index was then adjusted and fitted for each case, and the corresponding values are summarized in Fig. S6C.

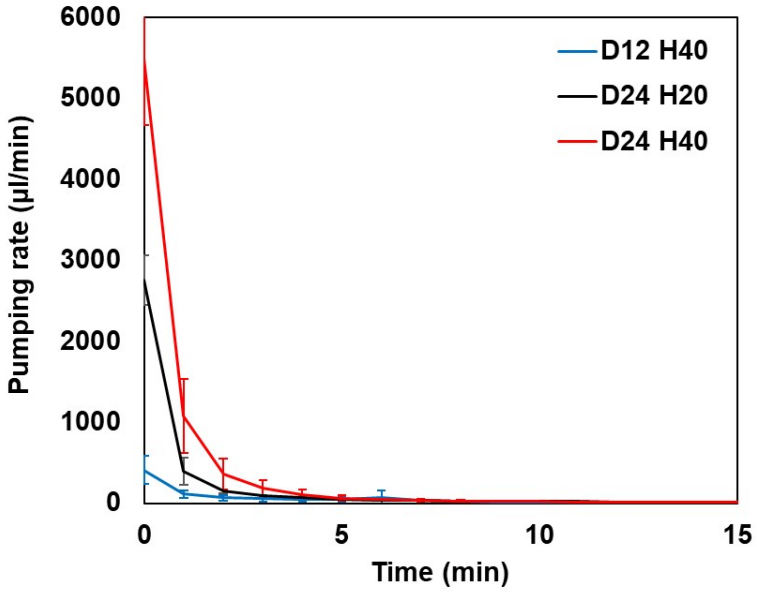

Figure S7. Pumping performance of AAG micropumps with various sizes.

S7. Pumping performance of AAG micropumps with various sizes.

The pumping rates of AAG micropumps with different sizes were compared, where *D* and *H* represent the diameter and height of the micropump in mm scale, respectively. The results showed that as the pump volume increased, the total amount of water absorbed also increased, along with a significant increase in the initial pumping rate. However, the increase in pump volume had no significant effect on extending the operational time compared to the utilization of flow resistor.

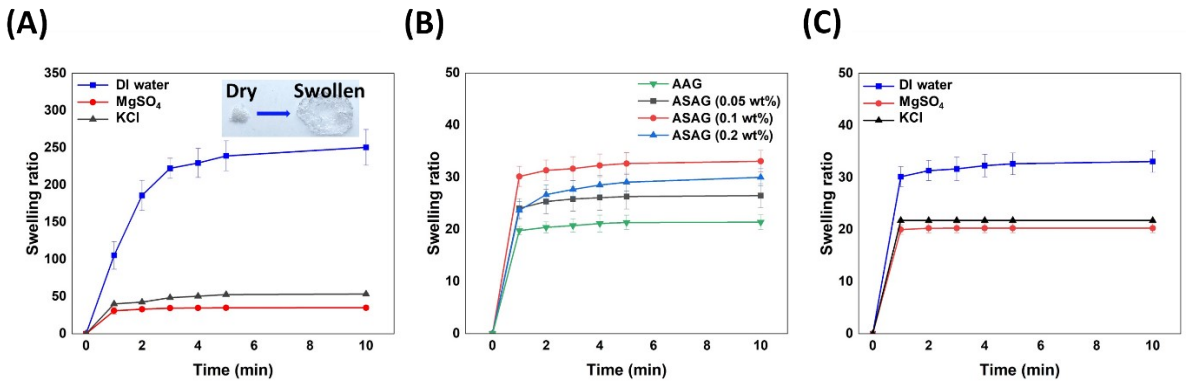

Figure S8. Comparison of swelling ratio of (A) sodium polyacrylate in DI water, $MgSO_4$, and KCl, (B) various concentrations of ASAG with that of AAG in DI water, (C) 0.1 wt% ASAG in DI water, $MgSO_4$, and KCl.

S8. Properties of superabsorbent polymer and ASAG

The swelling ratio of ASAG with various concentrations of SAP (0.05-0.2 wt%) was consistently higher than that of AAG (Fig. S8B). This enhancement was attributed to the embedded sodium polyacrylate, which rapidly absorbed water with high suction pressure upon contact with the water inside the porous network. Even with SAP concentration of 0.05 wt%, the maximum swelling ratio after 10 min increased to 26.5 compared with 21.4 for AAG. When the SAP concentration increased to 0.1 wt%, the swelling ratio after 10 min further improved to 33.1. However, a further increase in SAP concentration to 0.2 wt% resulted in a decreased swelling ratio of 30.0 at 10 min, likely due to the excessive SAP expansion, which hindered water permeability through the ASAG. For 0.05 and 0.01 wt% SAP concentrations, the swelling ratio reached its maximum within 10 min, whereas the 0.2 wt% ASAG did not achieve saturation until 20 min. Therefore, the 0.1 wt% SAP concentration, which had the highest maximum swelling ratio and fastest saturation time, was selected for the cylinder-shaped ASAG micropump. Furthermore, to demonstrate that SAP expansion reduced water permeability inside ASAG, the permeability coefficient of 0.1 wt% ASAG was measured and compared with that of AAG, exhibiting a decrease to 0.35 owing to the effect of SAP (Fig. S3B).

To further verify the effect of SAP on the ASAG pumping performance, the swelling ratio of ASAG in ionic solutions was measured and compared with that in DI water. The results showed a lower swelling ratio of 20.3 for $MgSO_4$ and 21.7 for KCl compared to 33.1 for DI water (Fig. S8C).